Smart protective coatings with self-sensing and active corrosion protection dual functionality from pH-sensitive calcium carbonate microcontainers

Liu, Tong; Zhang, Dawei; Ma, Lingwei; Huang, Yao; Hao, Xiangping; Terryn, Herman; Mol, Arjan; Li, Xiaogang

DOI
10.1016/j.corsci.2022.110254

Publication date
2022

Document Version
Final published version

Published in
Corrosion Science

Corrosion Science 200 (2022) 110254

Contents lists available at ScienceDirect

Corrosion Science

journal homepage: www.elsevier.com/locate/corsci

Smart protective coatings with self-sensing and active corrosion protection dual functionality from pH-sensitive calcium carbonate microcontainers

Tong Liu [a,b], Dawei Zhang [a,b,c,*], Lingwei Ma [a,b,c], Yao Huang [a,b], Xiangping Hao [a,b,c], Herman Terryn [d], Arjan Mol [e], Xiaogang Li [a,b,c]

[a] Beijing Advanced Innovation Center for Materials Genome Engineering, Institute for Advanced Materials and Technology, University of Science and Technology Beijing, Beijing 100083, China
[b] National Materials Corrosion and Protection Data Center, University of Science and Technology Beijing, Beijing 100083, China
[c] BRI Southeast Asia Network for Corrosion and Protection (MOE), Shunde Graduate School of University of Science and Technology Beijing, Foshan 528399, China
[d] Department of Materials and Chemistry, Research Group Electrochemical and Surface Engineering, Vrije Universiteit Brussel, Brussels, Belgium
[e] Department of Materials Science and Engineering, Delft University of Technology, Mekelweg 2, Delft 2628CD, The Netherlands

ARTICLE INFO

Keywords:
Corrosion
Organic coatings
Microcontainers
Corrosion sensing
Active corrosion protection

ABSTRACT

Herein, we report the development of a self-sensing and active corrosion protection coating which incorporates pH-sensitive multilayer chitosan/alginate-covered $CaCO_3$ microcontainers containing 1,10-phenanthrolin-5-amine (APhen). The microcontainers can respond to pH variation to release APhen which serves not only as a corrosion indicator but also as an inhibitor. An epoxy coating doped with 5 wt% microcontainers exhibited improved corrosion performance and was capable of inhibiting corrosion spreading from the damaged area in a 3.5 wt% NaCl solution. The salt spray test showed that corrosion damage can be quickly detected by the appearance of a red color within 2 min.

1. Introduction

Corrosion can cause catastrophic failures to metallic materials with substantial financial loss and serious negative impacts on structural integrity of load-bearing structures, ecological environment and industrial production [1,2]. Organic coatings are extensively applied to prevent metal substrates from corrosion by forming a physical barrier that isolates the metal from corrosive environments [3]. However, coating defects such as pinholes, cavities, cracks, mechanical scrapes, and scratches are inevitably formed during the coating preparation and service period. If undetected and untreated timely, these defects weaken the corrosion protection functionality of the coatings and can quickly develop into larger coating failures [4–6].

Early monitoring of corrosion may allow workers to repair or replace damaged coatings in time, thereby extending their lifetime of structures and reducing the risks of corrosion failure. Existing representative strategies to sense early under-film corrosion are mostly based on electrochemical [7], ultrasonic [8], electromagnetic [9], radiographic [10], and thermal imaging [11] systems. However, these methods are typically non-continuous, measurement techniques, costly and time-consuming and are often limited in the capability and resolution of detecting corrosion especially at very early stage. In recent years, self-sensing coatings capable of showing visible coloration triggered by mechanical or corrosion attacks have attracted increasing interest [5,12–16]. For example, Robb et al. reported a sensitive fluorescence-based method to automatically warn damage position in polymer materials through aggregation-induced emission (AIE) [17]. The AIE luminogen 1,1,2,2-tetraphenyl-ethylene (TPE) was encapsulated in polyurethane/poly(urea-formaldehyde) microcapsules. With the addition of 10 wt% microcapsules in the epoxy coating, the clear blue local fluorescence signals can appear within minutes when mechanical damage of the coating occurs in air. Besides, to achieve a coloration that can be observed with the naked eyes, a self-reactive visual microcapsule was prepared via encapsulating crystal violet lactone (CVL) in the polymethyl methacrylate (PMMA) shell with outer-surface-attached SiO_2 nanoparticles [18]. Shear, pressure and tensile forces imposed to the coating during damaging caused the microcapsules to rupture. The CVL flowed out of the ruptured PMMA shell to react with the SiO_2 to present a blue color for damage reporting. In addition, Liu et al. [19] developed a 1,10-phenanthrolin-5-amine modified polyurethane coating with

* Corresponding author at: Beijing Advanced Innovation Center for Materials Genome Engineering, Institute for Advanced Materials and Technology, University of Science and Technology Beijing, Beijing 100083, China.
E-mail address: dzhang@ustb.edu.cn (D. Zhang).

https://doi.org/10.1016/j.corsci.2022.110254
Received 4 October 2021; Received in revised form 26 January 2022; Accepted 16 March 2022
Available online 18 March 2022

intrinsic self-healing property endowed by the dynamic hydrogen bonds in the backbone of the resulting elastomeric network. The immersion test indicates that the occurrence of early corrosion (~5 mins) can be visualized by the formation of APhen-Fe^{2+} ligands with a red color and the presence of hydrogen bonds also endowed the coating matrix with a certain self-healing effect (60% of the tensile strength recovery) in a salt water environment. In another study, Wilhelm et al. prepared corrosion-sensing nanoadditives based on layered double hydroxides (LDHs) intercalated with hexacyanoferrate [16]. The aqueous dispersion of hexacyanoferrate-intercalated LDHs turned blue in the presence of Fe^{2+}. When in contact with corrosive solution, the formation of the blue precipitate was observed on the carbon steel surface after a few minutes of exposure.

Besides damage/corrosion-sensing ability, active corrosion protection ability is also a favorable property for the development of smart protective coatings used in harsh service environments where repair or replacement may be difficult and/or costly. Active corrosion protection coatings can repair the corrosion damages and/or inhibit corrosion deterioration with minimal or no external intervention [20]. The active protection process of these smart coatings could be achieved by the release of healing agents such as polymerizable materials [21,22] or corrosion inhibitors [23,24] which through various encapsulation technologies could be conveniently released when triggered by different conditions (light [25,26], pH [27,28], humidity [29], temperature [30] or ions [31]). Among the encapsulation technologies for healing agents that have been applied to the active corrosion protection coatings, the layer-by-layer (LbL) self-assembly approach is a prominent one [32–34]. For example, Shchukin's group had applied this technique to assemble the nanocontainers of corrosion inhibitors for self-healing coatings via alternate deposition of oppositely charged polyelectrolytes or inhibitors onto the surface of silica nanoparticles [35–40]. The obtained nanocontainers can intelligently release the pre-embedded corrosion inhibitors during corrosion because the permeability of polyelectrolyte multilayers can be changed by local pH variation.

In view of the benefits associated with damage/corrosion-sensing and active corrosion protection capabilities, combining the two functions into the same coating would bring about several useful features for corrosion protection, including (1) rapid identification of corrosion location; (2) controlled releases of healing agents as induced by environmental stimuli; (3) active corrosion protection after damage. Herein, this work reports a smart protective coating possessing both damage warning and active corrosion protection abilities, enabled by pH-sensitive chitosan/alginate@$CaCO_3$ (CA@Ca) microcontainers containing 1,10-phenanthrolin-5-amine (APhen) molecules. When corrosion occurs on the steel substrate, the produced Fe^{2+} ions can quickly react with the released APhen from CA@Ca-APhen microcontainers to produce a pronounced red color for visual early warning. Meanwhile, the APhen molecules can adsorb on the steel substrate to suppress the corrosion activities within the coating scratch. The chemical composition of the CA@Ca-APhen microcontainers was characterized by Fourier transform infrared spectroscopy (FTIR). Scanning electron microscope (SEM) and transmission electron microscopy (TEM), nitrogen adsorption isotherms and Zeta potential measurement were conducted to verify the successful synthesis of the microcontainers. Moreover, the UV–vis spectroscopy confirmed that the APhen molecules in the CA@Ca-APhen microcontainers could be effectively released under increased acidity or alkalinity. Electrochemical impedance spectroscopy (EIS) was used to evaluate the corrosion inhibition effect of the CA@Ca-APhen microcontainers and the active corrosion protection performance of the coating. The corrosion sensing ability of the coating was studied by exposure of the coated steel to the neutral salt spray test.

2. Experimental

2.1. Materials

Calcium chloride ($CaCl_2$, 99.5%), sodium carbonate (Na_2CO_3, 99.5%), sodium dodecyl sulphate (SDS, 99.0%), sodium chloride (NaCl, 99.0%), chitosan, alginate, sodium hydroxide (NaOH), acetic acid (99.7%), hydrochloric acid (HCl, 36.0%) and 1,10-phenanthrolin-5-amine (APhen) (98.0%) were purchased from Aladdin industrial corporation. Epoxy resin 51 (E51) and the curing agent (polyetheramine D400) were provided by Jiangsu Heli resin Co., Ltd. All chemicals were used without further purification. The Q235 steel (99.09% Fe, 0.21% C, 0.45% Mn, 0.18% Si, 0.03% S and 0.04% P) was selected as the substrate for the coatings. The steel samples were abraded sequentially with 240, 400, and 800 grit abrasive papers. The steel samples were dried in air after being washed via deionized water and ethanol.

2.2. Synthesis of the microcontainers and loading of APhen

The $CaCO_3$ microcontainers were synthesized according to a previous study [41]. Briefly, Na_2CO_3 (3.5 g, 33.0 mmol) and SDS (0.5 g, 1.8 mmol) were fully dissolved in 100 mL deionized water. Then, $CaCl_2$ (3.7 g, 33.0 mmol) in 100 mL deionized water was added into the aforementioned solution under stirring for 20 min at 25 ℃. The mixture was kept under stagnant conditions for 30 min and the supernatant was removed. Afterward, the final products were washed with deionized water and dried in a vacuum oven at 50 ℃ for 24 h.

For drug loading, the aqueous APhen solution (1.5 mg mL^{-1}) was introduced into the $CaCO_3$ microcontainers using a vacuum loading method (vacuum pressure of −0.1 MPa for 6 h) at 25 ℃. The as-prepared $CaCO_3$ microcontainers containing APhen (Ca-APhen) were centrifuged at 6000 rpm for 5 min. The Ca-APhen/water slurry was directly used for the encapsulation process in the following section. The dry content of the Ca-APhen in the $CaCO_3$-APhen/water slurry, obtained by comparing the weights of the slurry before and after drying in a vacuum oven at 50 °C, was ~72.3 wt%.

2.3. Encapsulation by chitosan/alginate multilayers

Chitosan/alginate multilayers were assembled to the Ca-APhen

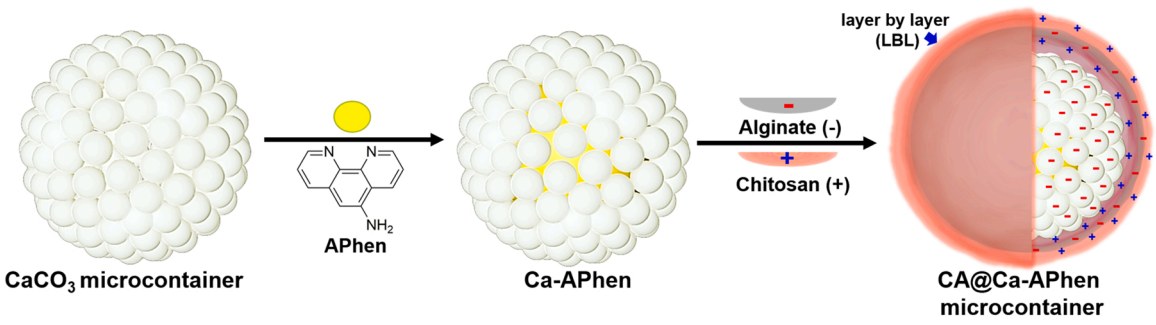

Fig. 1. Schematic illustration of the preparation procedure of the CA@Ca-APhen microcontainer.

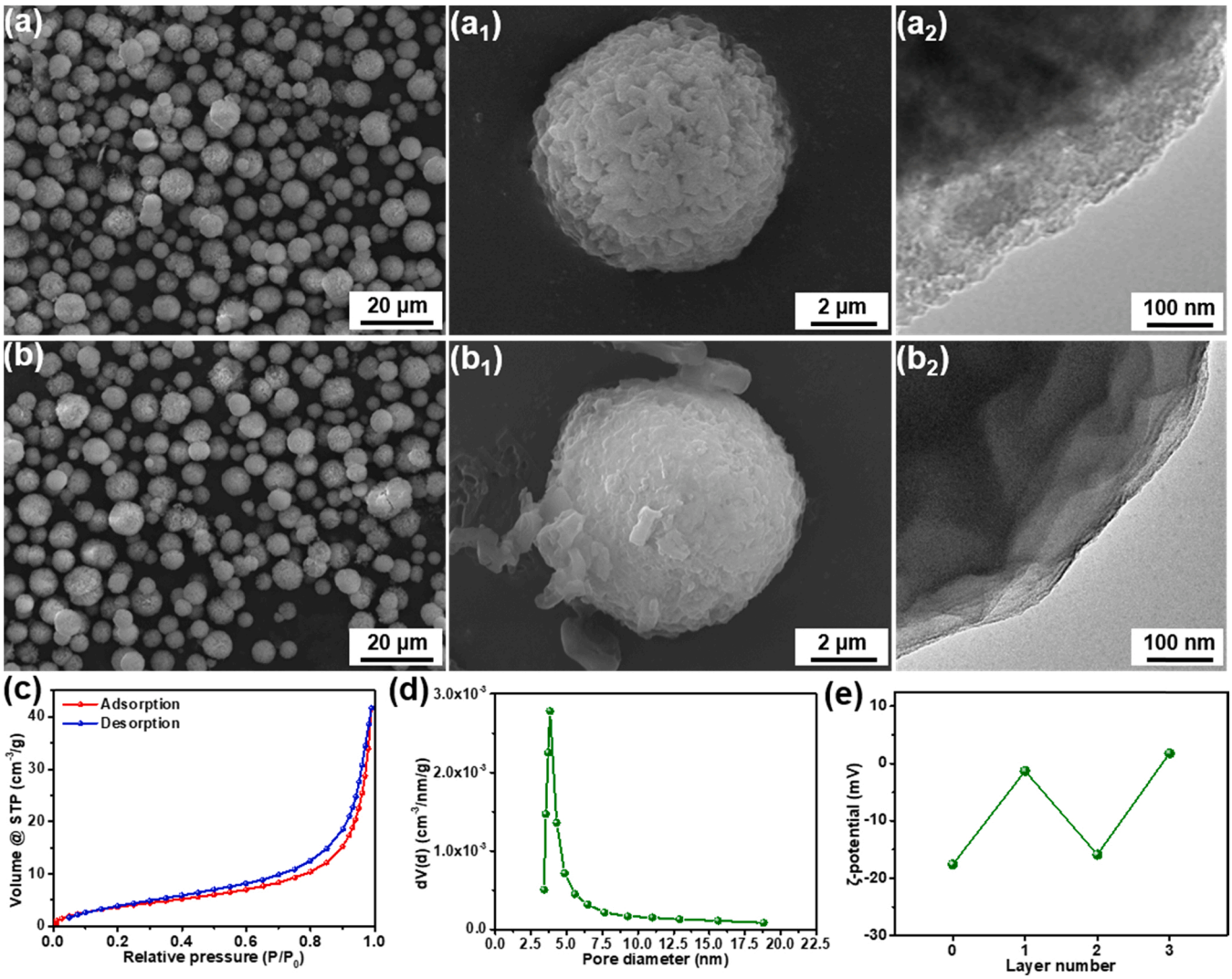

Fig. 2. SEM images of (a, a_1) $CaCO_3$ microcontainers and (b, b_1) CA@Ca-APhen microcontainers; TEM images of edge position of (a_2) $CaCO_3$ microcontainers and (b_2) CA@Ca-APhen microcontainers; (c) N_2 adsorption-desorption isothermal curve of $CaCO_3$ microcontainers; (d) the pore size distribution of $CaCO_3$ microcontainers; (e) Changes of ζ-potential during the LbL deposition, Layer 0: initial Ca-APhen; Layer 1: Ca-APhen/chitosan; Layer 2: Ca-APhen/chitosan/alginate; Layer 3: Ca-APhen/chitosan/alginate/chitosan.

surface via a LbL deposition method. Initially, the solutions of chitosan (2.0 mg mL^{-1}) and alginate (2.0 mg mL^{-1}) were prepared in 5 wt% of acetic acid aqueous solution and deionized water, respectively. The pH value of the chitosan solution was adjusted to 4.8 using a 0.1 M HCl solution, producing a positive net charge on the chitosan molecules. The pH of the alginate solution was adjusted to 6.0 using a 0.1 M NaOH solution to induce negative charges on alginate. For the adsorption of the first layer, Ca-APhen dispersion liquid (50 mL, 5.0 mg mL^{-1}) was mixed with chitosan solution (10 mL, 2.0 mg mL^{-1}). The Ca-APhen/chitosan sample was washed with deionized water and collected by centrifugation. The washing process was repeated twice to remove the excess polyelectrolyte impurities. Next, the deposition of the alginate layer was conducted via mixing 20 mL of 2.0 mg mL^{-1} alginate solution with the centrifuged Ca-APhen/chitosan sample. The Ca-APhen/chitosan/alginate sample was washed with deionized water and separated via centrifugation. Then the third layer was assembled using the same process described for the first layer. The final structure of microcontainers was Ca-APhen (−)/chitosan (+)/alginate (−)/chitosan (+), marked as CA@Ca-APhen microcontainer. The CA@Ca-APhen microcontainers were separated via centrifugation and washed with deionized water twice. Finally, the microcontainers were collected after drying at 50 °C. Fig. 1 depicts the preparation procedure of the CA@Ca-APhen microcontainer.

2.4. Preparation of composite coatings

Composite coatings containing 2.5, 5.0, and 7.5 wt% of CA@Ca-APhen microcontainers were prepared on the surface of the Q235 steel substrate using a procedure as follows. The CA@Ca-APhen microcontainers were dispersed into the E51 resin using a mechanical agitator rotating at 500 rpm for 1 h, followed by the addition of the D400 curing agent (molar ratio: E51/D400 = 5/3). The obtained mixture was applied on the surface of the steel sample by a bar coater. Then the coated samples were dried at 25 ℃ for 48 h to obtain the CA@Ca-APhen epoxy composite coating (CA@Ca-APhen/EP). The neat epoxy coating was prepared by the same method in absence of CA@Ca-APhen microcontainers. The thickness of all coatings was approximately 60 μm.

2.5. Characterization

The morphology of the samples was observed using SEM (ZEISS Gemini 300) and TEM (FEI Tecnai G2 F20). The pore size distribution and pore volume of the synthesized containers were investigated by

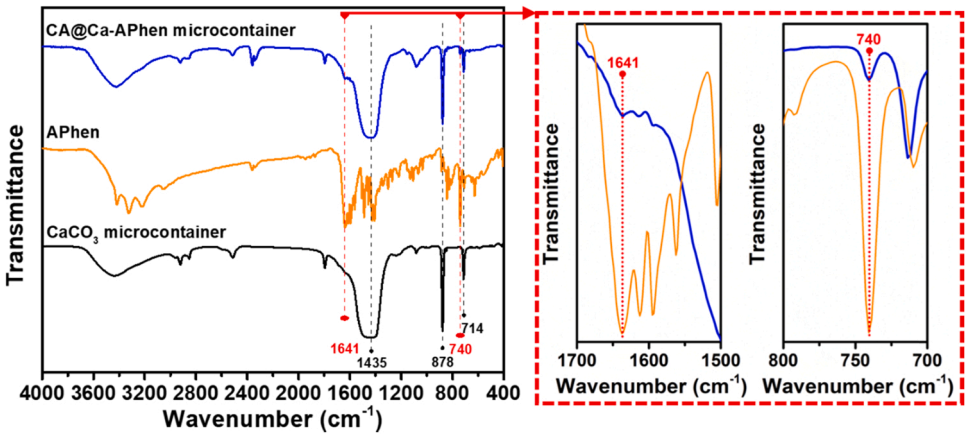

Fig. 3. FTIR spectra of APhen, $CaCO_3$ microcontainer, and CA@Ca-APhen microcontainer.

nitrogen adsorption isotherms (Brunauer Emmett Teller, BET, Michael ASAP2460). The corrosion inhibition effect and surface roughness of the CA@Ca-APhen microcontainers were investigated by Leica TCS PS8 X confocal laser scanning microscopy (CLSM). The FTIR spectra of the synthesized samples and APhen were performed with a Bruker Vertex 70 spectrometer from 4000 to 400 cm^{-1}. The Fe^{2+}-APhen complex and its distribution were determined by Raman spectroscopy (LabRam HR Evolution). The changes of ζ-potential of Ca-APhen microcontainers during the LbL deposition were monitored using a Malvern Zetasizer Nano ZS Instrument. The loading capacity and release curves of APhen in CA@Ca-APhen microcontainers were obtained by UV–vis spectroscopy (PE, Lambda1050) according to the method described previously [42,43]. Thermal analysis of samples was performed using Netisch thermo gravimetric analysis (TGA).The tempearture ranged from 30 to 800 ℃ at a heating rate of 10 ℃/min under N_2 atmosphere to examine the thermal degradation behavior of the APhen, $CaCO_3$ microcontainer, CA@Ca microcontainer, and CA@Ca-APhen microcontainer.

To investigate the corrosion protection properties, EIS measurements were performed in a 3.5 wt% NaCl solution on the bare steel, the scratched and the intact coatings applied on the steel. In the EIS test, the exposed area of the coated samples was 1 cm^2. The EIS results were obtained with a PARSTAT 2273 electrochemical station with a three-electrode cell system employing the sample substrate as a working electrode, a saturated calomel electrode (SCE) as a reference electrode, and a platinum plate electrode as a counter electrode. The EIS data were measured in the frequency range (10^{-2}-10^5 Hz) with an amplitude of 20 mV. The tests were conducted on duplicate samples to verify the reliability and reproducibility of data. In addition, to obtain the inhibition efficiency of released APhen on the bare steel substrate (testing area: 1 cm^2) in the 60 mL 3.5 wt% NaCl solution, potentiodynamic polarization curves were obtained in the potential region of ± 250 mV around the OCP at a scanning rate of 1 mV/s. To avoid supersaturation of the tested solution, the content of CA@Ca-APhen microcontainers was maintained at 100 mg/L.

The water-uptake of the coating ($X_{vol\%}$) can be obtained from the coating film capacitance, using the following equation [44,45]:

$$X_{vol\%} = \frac{\log[f_0](\frac{C_f(t)}{C_f(0)})}{\log[f_0](80)} \times 100 \quad (1)$$

where $C_f(t)$ and $C_f(0)$ represent the coating film capacitance at tested time t and initial time, respectively.

To further study the self-sensing and active corrosion protection performance of the selected coatings, the coated steels were exposed to 3.5 wt% NaCl salt spray for 720 h according to ASTM D1654.

Pull-off tests were carried out on original samples and the ones after 720 h of salt spray corrosion test to compare dry and wet adhesion strengths. According to ASTM D4541 standard, five aluminum test dollies were bonded onto the coating surface using a two-part Araldite 2015 adhesive (Huntsman Advanced Materials, Germany). The samples were then left at 50 ℃ for 24 h to ensure the adhesive is fully cured. Before pull-off measurements, the test area was isolated from the bulk intact coating using a cutting tool. The pulling force was exerted normally to the coated surface until the coating was detached from the substrate (the pulling speed was set to 10 mm/min).

3. Results and discussion

3.1. Synthesis and characterization of CA@Ca-APhen microcontainers

The morphology of the $CaCO_3$ microcontainers before and after chitosan/alginate encapsulation are studied by SEM. In Fig. 2a, the $CaCO_3$ microcontainers display a spherical shape with a diameter of 2–8 μm. The high-resolution SEM image in Fig. 2a_1 shows the porous surface of a single $CaCO_3$ microcontainer. In Fig. 2a_2, the TEM image further reveals the ultrafine porous structure at the outer surface of the $CaCO_3$ microcontainers. Furthermore, in Fig. 2c, the isotherms of the $CaCO_3$ microcontainers belong to the type Ⅳ isotherm with H3 type hysteresis loop, which confirms the formation of mesoporous structures in the microcontainers [46,47]. The pore sizes of the $CaCO_3$ microcontainers are mostly around ~4 nm (Fig. 2d). Calculated by the N_2 adsorption/desorption isothermal curves, the average pore diameter and pore volume of the $CaCO_3$ microcontainers were 3.8 nm and 6.3×10^{-2} cm^3 g^{-1}, respectively (Figs. 2c, 2d), indicating a good drug-loading capacity of this container. After the loading of APhen and the encapsulation by chitosan/alginate polyelectrolyte multilayers, the CA@Ca-APhen microcontainers present a similar size to the $CaCO_3$ microcontainers without any agglomeration (Fig. 2b). As shown in Fig. 2b_1, the modification by the polyelectrolyte resulted in a smooth surface of the CA@Ca-APhen microcontainers. To verify the interaction between the $CaCO_3$ microcontainers and the chitosan/alginate multilayers, Fig. 2e shows the ζ-potential values of the microcontainers after the assembly of each polyelectrolyte layer. The corresponding surface morphologies of the microcontainers are shown in Fig. S1. The ζ-potential of the initial Ca-APhen microcontainers is − 17.6 mV. After deposition of the first chitosan layer, the surface charge of the microcontainer increased to − 1.3 mV and the microcontainer surface (Fig. S1b) became smoother than the original surface (Fig. S1a). However, the coverage of the chitosan layer on the microcontainer surface was probably not uniform since the potential did not become positive. The subsequent deposition of the first alginate layer decreased the ζ-potential to − 15.9 mV and resulted in a relatively smooth surface of the microcontainer (Fig. S1c). After the final chitosan layer was assembled, the ζ-potential of the microcontainers increased to 1.8 mV.

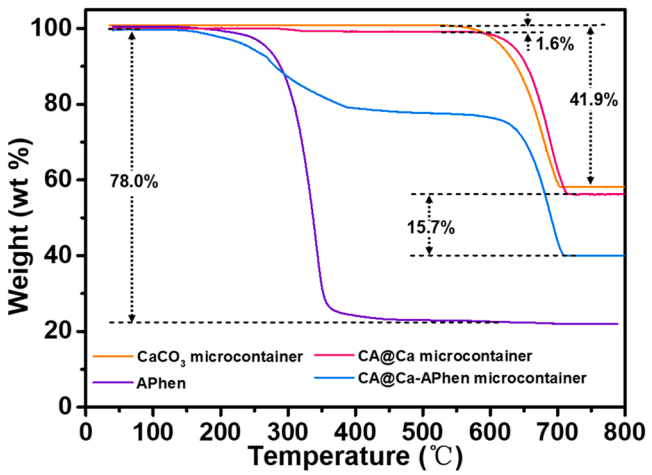

Fig. 4. TGA curves of APhen, $CaCO_3$ microcontainer, CA@Ca microcontainer, and CA@Ca-APhen microcontainer.

These observations indicate that the assembly of the $CaCO_3$ microcontainers and the chitosan/alginate polyelectrolyte multilayers is mainly driven by the electrostatic interactions of the adjacent surface/layers with opposite electrical charges. The TEM images (Fig. 2b$_2$) and SEM (Fig. S1d) further confirm that the surface of the microcontainer has been successfully covered by the chitosan/alginate polyelectrolyte multilayers.

FTIR was employed to confirm the encapsulation of APhen. Fig. 3 shows the FTIR spectra of the $CaCO_3$ microcontainer, APhen, and CA@Ca-APhen microcontainer. For $CaCO_3$ microcontainers and CA@Ca-APhen microcontainers, the strong bands at 714, 878 and 1435 cm^{-1} are associated with the ν_2, ν_3 and ν_4 characteristic vibrations of the carbonate in $CaCO_3$, respectively [48]. Notably, two new peaks are found at 740 and 1641 cm^{-1} for CA@Ca-APhen microcontainers, which are assigned to the C–H out-of-plane bending vibration and the C=N stretching vibration of the phenyl ring in APhen molecules, respectively [49]. Prior to the FTIR test, the synthesized CA@Ca-APhen powder has been repeatedly washed with deionized water, which eliminates the interference of the free APhen. This result confirmed the successful loading of APhen in the $CaCO_3$ microcontainers.

Thermogravimetric analysis (TGA) was used to estimate the amount of APhen loaded in the CA@Ca-APhen microcontainers. Fig. 4 depicts the TGA curves of APhen, $CaCO_3$ microcontainer, CA@Ca microcontainer, and CA@Ca-APhen microcontainer. For the $CaCO_3$ microcontainer, a weight loss of 41.9 wt% is observed between 600 ℃ and 700 ℃, which could be attributed to the decomposition of calcium carbonate into CaO and CO_2 [50]. In the TGA curve of the CA@Ca microcontainer, a weight loss of 1.6 wt% is observed from 283 °C to 600 °C, which possibly corresponds to the decomposition of the chitosan/alginate multilayers [50,51]. Compared with the TGA curve of the CA@Ca microcontainer, the curve of the CA@Ca-APhen shows a 15.7 wt % weight loss at 200–700 °C which is attributed to the decomposition of APhen molecules [52,53]. This was consistent with the results obtained from the TGA curve of APhen. The weight loss of APhen reaches 78.0 wt % as the temperature increases to 700 °C, and the remaining 22.0 wt% of the weight is associated with carbon residues. Therefore, the content of APhen in CA@Ca-APhen, estimated by dividing 15.7 wt% by 78.0 wt %, is approximately 20.1 wt%.

Generally, a pH-sensitive smart container system is capable of blocking corrosion inhibitor leaching in the near-neutral pH condition, while releasing corrosion inhibitor in acidic and alkaline pH conditions. The corrosion of the damaged area for coated steel in neutral NaCl solution results in the variation of pH because of anodic and cathodic reactions [54]. The local pH change triggers the opening or the closure of the chitosan/alginate polyelectrolyte shell [55]. Figs. 5a and 5b shows the cumulative release of the APhen molecules from Ca-APhen microcontainers and CA@Ca-APhen microcontainers under pH values from 4 to 10, which is a common pH range caused by corrosion in a coating defect [56,57]. Without the encapsulation by the chitosan/alginate multilayers, over 60% of the APhen molecules loaded in the Ca-APhen microcontainers were released after 5 min under different pH conditions. In particular, the cumulative release of APhen reached 82.5% after 5 min at pH = 4. This accelerated release may be attributed to the decomposition of the $CaCO_3$ under acidic conditions. As shown in Fig. 5a, the APhen in the Ca-APhen microcontainers was completely released after 3 h of immersion under all pH conditions, which suggests that without encapsulation the APhen loaded in microcontainers is prone to leakage at an early stage. For the CA@Ca-APhen microcontainers (Fig. 5b), the release curves exhibit three stages including the initial fast release (stage 1) stage, the sustainable release (stage 2) stage and the plateau stage (stage 3). The release of APhen is dependent on the pH value of the solution. Under neutral conditions (pH = 7), only 62.1% of APhen was released from the microcontainers after 24 h, demonstrating that CA@Ca-APhen microcontainers can successfully suppress the spontaneous leaching of APhen. At the acidic pH, the release rate and maximum amount of APhen released was significantly increased. The accumulative amount of the released APhen was 77.9% after 24 h. At pH = 10, the release of APhen was even more significantly accelerated and increased in its maximum amount released. After 24 h immersion, about 96.5% of the loaded APhen was released from the microcontainers, revealing that the CA@Ca-APhen microcontainers can release APhen in a highly pH-sensitive manner. These results confirm that the CA@Ca-APhen microcontainer can provide a smart release on demand whenever pH change occurs at localized regions as a result of corrosion of the Q235 steel.

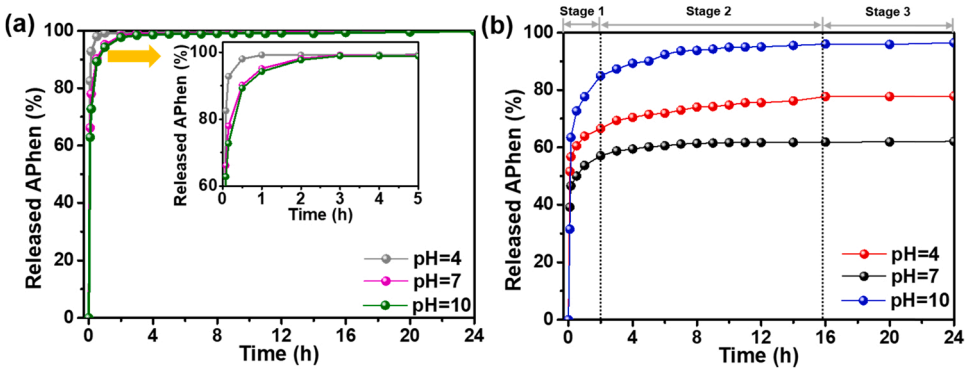

Fig. 5. The release curves of APhen molecules from (a) Ca-APhen microcontainers and (b) CA@Ca-APhen microcontainers at different pH conditions in 3.5 wt% NaCl solution.

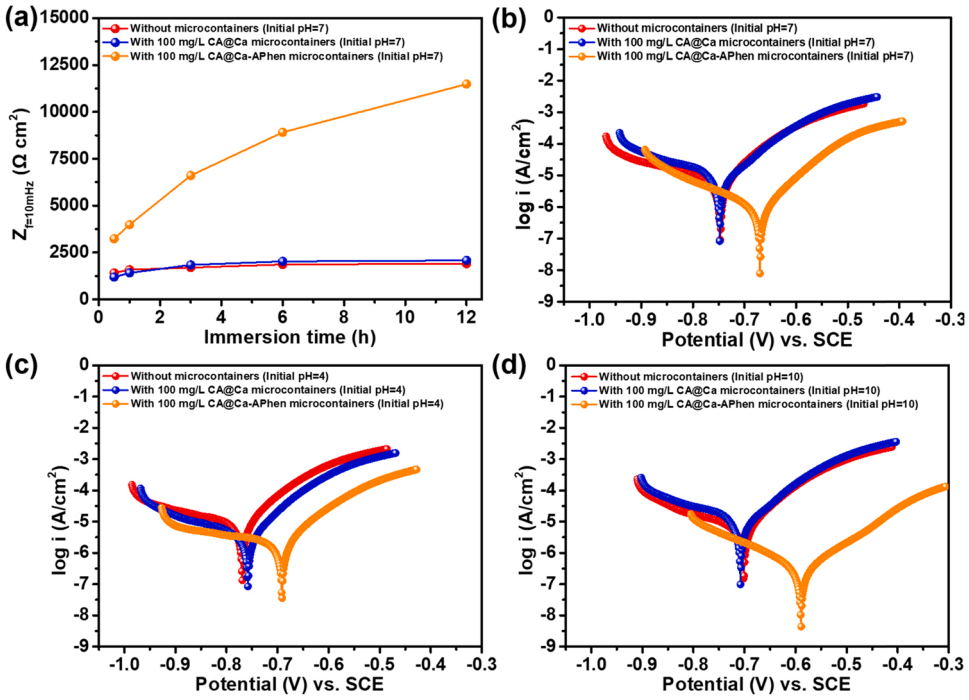

Fig. 6. (a) The variation of $|Z|_{f=10mHz}$ values versus immersion time and (b-d) the polarization curves for the steel after 12 h immersion in the 3.5 wt% NaCl solution with different pH (no microcontainers added; CA@Ca microcontainers added; CA@Ca-APhen microcontainers added).

3.2. Corrosion inhibition by CA@Ca-APhen microcontainers

To study the corrosion inhibition effect of the APhen molecules released from CA@Ca-APhen microcontainers on the Q235 steel substrate, EIS measurements were carried out in 3.5 wt% NaCl solution in the absence or the presence of microcontainers (Fig. S2a, b, c). It is generally accepted that for metal substrates exposed to NaCl based aqueous electrolytes without/with inhibitors, the impedance modulus at 10 mHz ($|Z|_{f=10mHz}$) of the Bode plots can be used as a semi-quantitative indicator of the corrosion susceptibility of the metal substrate, with higher impedance modulus values indicating a higher corrosion resistance [20]. Fig. 6a shows the variation of the $|Z|_{f=10mHz}$ values with time for the steel specimens immersed in the solutions without microcontainers (blank system), with the addition of CA@Ca microcontainers

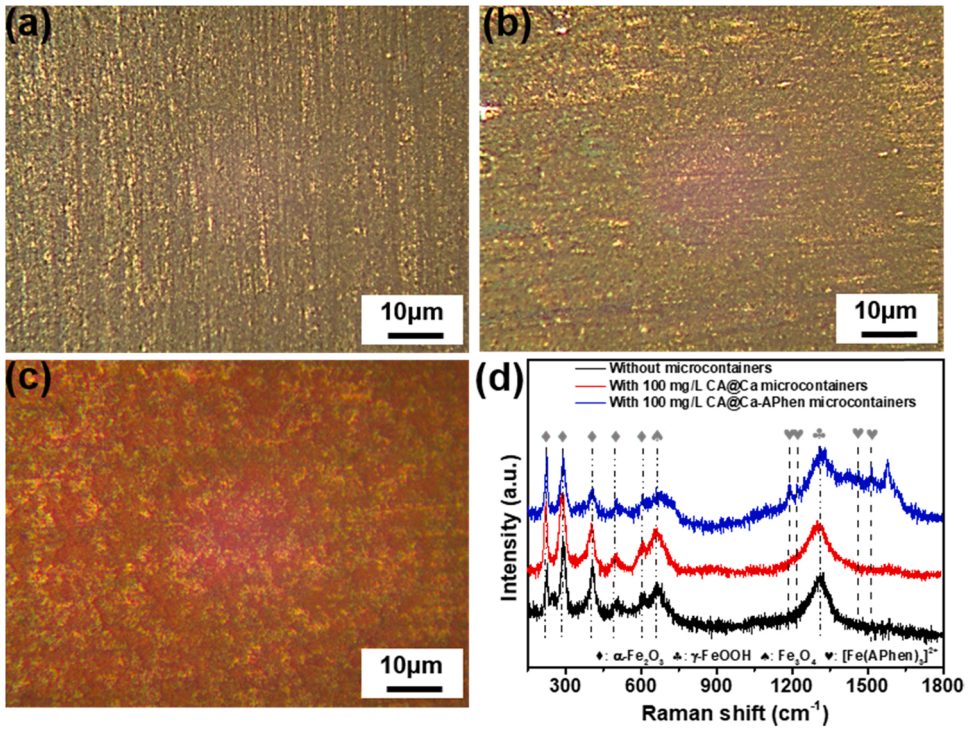

Fig. 7. Optical images of the steel surface after 24 h of immersion in the 3.5 wt% NaCl solution (not derusted) with (a) no microcontainers added, (b) CA@Ca microcontainers added, (c) CA@Ca-APhen microcontainers added; (d) corresponding Raman spectra of the steel surfaces.

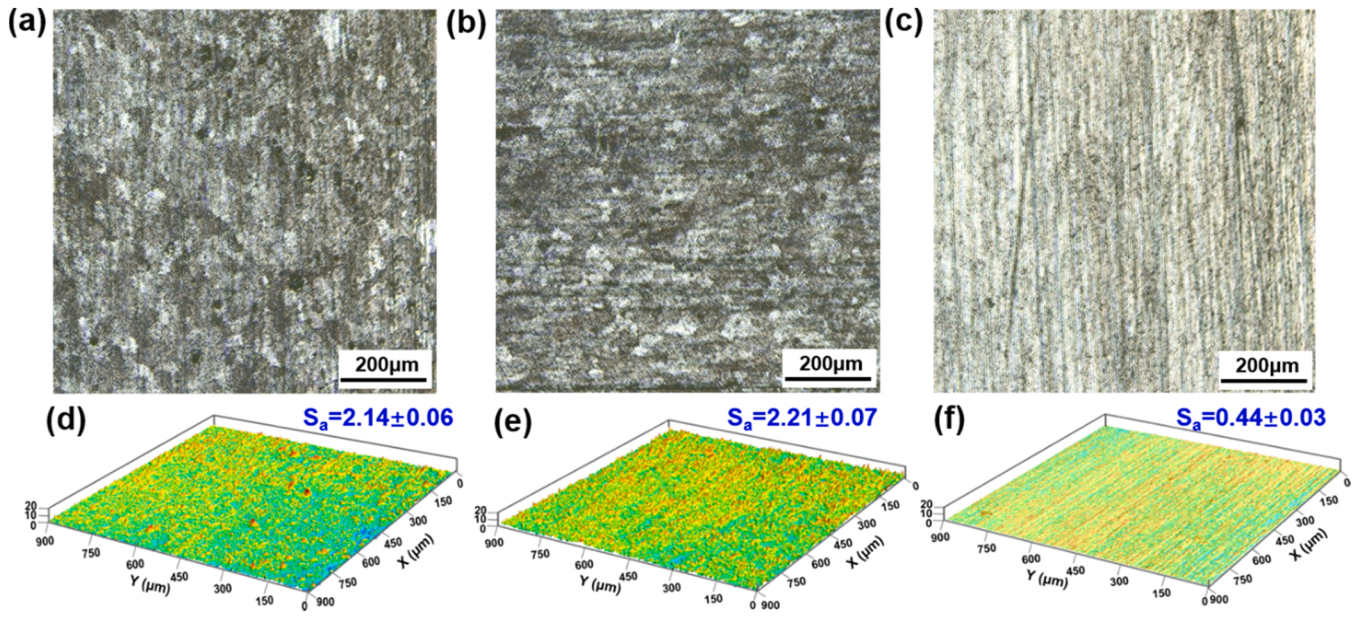

Fig. 8. Optical images and CLSM images of the steel surfaces after 24 h of immersion in the 3.5 wt% NaCl solution (derusted) with (a and d) no microcontainers added; (b and e) CA@Ca microcontainers added; (c and f) CA@Ca-APhen microcontainers added.

and with the addition of CA@Ca-APhen microcontainers. It can be observed that the presence of CA@Ca-APhen microcontainers induced a remarkable increase of the $|Z|_{f=10mHz}$ value in comparison to the blank system or that with the CA@Ca microcontainers. This value continued to increase from 3.23×10^3 Ω cm^2 to 1.15×10^4 Ω cm^2 as the immersion time increased. Furthermore, potentiodynamic polarization test was used to evaluate corrosion of the Q235 steel specimen and the corrosion inhibition effect of CA@Ca-APhen microcontainers after 12 h immersion in the 3.5 wt% NaCl solution at different initial pH values (4, 7, 10) (Fig. 6b-d). Compared to the curves for the blank system or the ones for the steels with CA@Ca microcontainers, the polarization curves (particularly the anodic branches) for the steels with CA@Ca-APhen microcontainers shifted to regions with lower current densities at all pH conditions, suggesting that the anodic corrosion reactions were suppressed. Besides, the specimens in the presence of CA@Ca microcontainers showed similar results of the EIS and polarization tests to those of the blank system, indicating that the corrosion inhibition effect was indeed from APhen not the CA@Ca microcontainers (100 mg/L).

To further study the adsorption behavior and the inhibition effect of APhen, the optical images and 3D morphologies of Q235 steel surface after 24 h immersion in 3.5 wt% NaCl solution without microcontainers (blank system), with the addition of CA@Ca microcontainers and with the addition of CA@Ca-APhen microcontainers were shown in Fig. 7a-c (not derusted). In Figs. 7a and 7b, the Q235 steel surface was covered with a significant amount of corrosion products. In the presence of CA@Ca-APhen microcontainers (Fig. 7c), the steel surface shows a red color uniformly. Fig. 7d shows the chemical composition of the steel surface after 24 h of immersion in the 3.5 wt% NaCl solution under the different situations. For the steel without microcontainers and the steel with the addition of CA@Ca microcontainers, the main components are α-Fe_2O_3 (225, 292, 408, 501 and 611 cm^{-1}), Fe_3O_4 (662 cm^{-1}), and γ-FeOOH (1317 cm^{-1}) [58,59]. In contrast, the new feature bands at 1188, 1213, 1461 and 1513 cm^{-1} are observed on the Q235 steel surface in the presence of the CA@Ca-APhen microcontainers and can be attributed to the generation of the Fe^{2+}-APhen complex ($[Fe(APhen)_3]^{2+}$) [24].

To verify the corrosion inhibition effect of the CA@Ca-APhen microcontainers, we removed the rust layer and then compared the steel surfaces of different situations (Fig. 8). In Figs. 8a and 8b, the steel surfaces were rough and covered with severe corrosion pits. In comparison, only slight corrosion was seen for the steel surface when the CA@Ca-APhen microcontainers were present (Fig. 8c). According to the CLSM measurements, the surface roughness (S_a) values of the steel surfaces after immersion in the blank solution and the solution coating CA@Ca microcontainers were 2.14 (Figs. 8d) and 2.21 (Fig. 8e), respectively. In contrast, in Fig. 8f, a much lower S_a value (0.44) was observed for the steel in the presence of the CA@Ca-APhen microcontainers. From these results, we can infer that the released APhen from CA@Ca-APhen microcontainers can effectively inhibit corrosion of the steel surface.

3.3. Barrier performance of the CA@Ca-APhen/EP coatings

In practice, the inherent barrier performance of the coating is critical to the service life of the coating at intact regions. To this end, EIS analyses were used to study the electrochemical behavior and the barrier properties of the intact coatings containing CA@Ca-APhen microcontainers. Fig. 9a-h shows the Nyquist and Bode plots of the coatings immersed in 3.5 wt% NaCl solution for different time. In Fig. 9a, the Nyquist plot of the neat epoxy coating presents a rapid decrease in the size of the semi-circle over time, indicating a weak corrosion protection capability. Two time constants can be observed after 40 days of immersion, suggesting that the corrosive species had reached the coating/steel interface. In contrast, for all coatings incorporating CA@Ca-APhen microcontainers, the reduction in the size of the semi-circle was significantly suppressed. Only one time constant can be found for the three composite coatings containing CA@Ca-APhen microcontainers during the 60 days of immersion (Figs. 9c, e, g), indicating an improved barrier performance. For the Bode plots, the $|Z|_{f=10mHz}$ values of neat epoxy coating declined from 2.32×10^{10} Ω·cm^2 continuously to 8.13×10^7 Ω·cm^{2}during the 60 days of immersion (Fig. 9b), which could be attributed to the pinholes and micro-defects in the coating. For the three composite coatings with the CA@Ca-APhen microcontainers, despite the decreasing trends over time, the $|Z|_{f=10mHz}$ values of the coatings remained higher than 10^9 Ω·cm^2 even after 60 days of immersion (Figs. 9d, f, h). Compared with the neat epoxy and the other two composite epoxy coatings, the $|Z|_{f=10mHz}$ value of the coating containing 5 wt% CA@Ca-APhen microcontainers declined from 6.92×10^{10} to 9.77×10^9 Ω·cm^2 during 60 days immersion (Fig. 9f), demonstrating enhanced long-term corrosion protection performance. In addition, it is

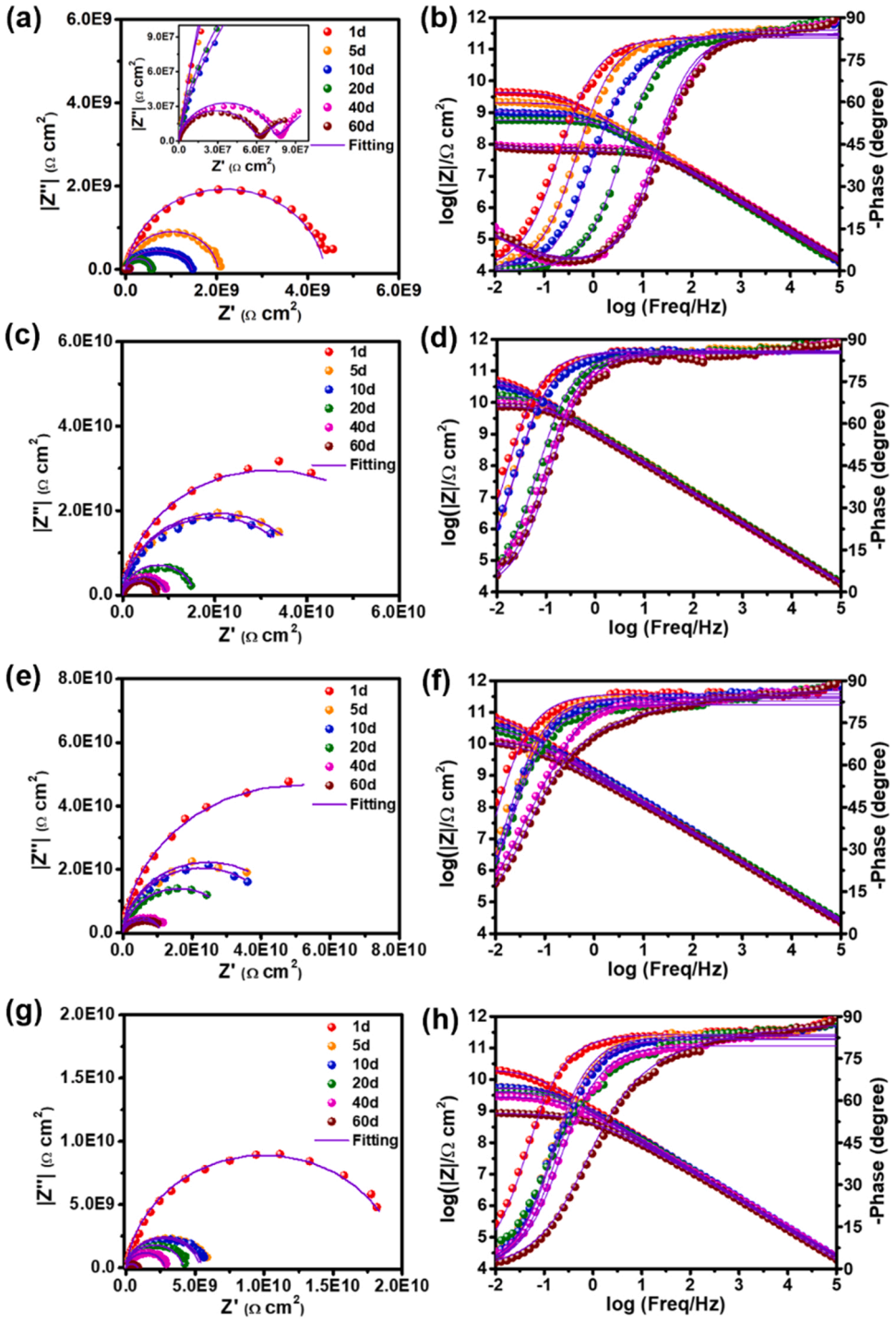

Fig. 9. Nyquist plots and Bode plots of intact neat epoxy coating (a and b), CA@Ca-APhen$_{2.5\ wt\%}$/EP coating (c and d), CA@Ca-APhen$_{5\ wt\%}$/EP coating (e and f) and CA@Ca-APhen$_{7.5\ wt\%}$/EP coating (g and h) during immersion in 3.5 wt% NaCl solution for 60 days.

worth noting that the impedance moduli of the coating containing 7.5 wt% CA@Ca-APhen microcontainers are lower than that of the coatings with the addition of 2.5 wt% and 5 wt% CA@Ca-APhen microcontainers (Figs. 9d and h). This may be attributed to the fact that the addition of an excess amount of fillers could introduce additional defects as diffusional pathways for corrosion species in the coating matrix (Fig. S3).

The EIS results of the intact coating were fitted by equivalent electrical circuits. The solution resistance (R_s), pore resistance (R_{po}), charge transfer resistance (R_{ct}), non-ideal film capacitance (CPE_f) and non-ideal double-layer capacitance (CPE_{dl}) parameters are contained in the circuits. At the early stage of immersion, the corrosion species permeate into the coating matrix through the intrinsic porosity of the epoxy matrix. This electrochemical process could be fitted by Circuit I in Fig. 10a. When the electrolyte has reached the coating/steel interface and charge transfer at the steel substrate occurred, a new peak shows up in the high frequency region (Fig. 10b, the Bode plots after 40 days of immersion). Therefore, R_{ct} and Q_{dl} were included and Circuit II was used for fitting. Furthermore, the water-uptake values ($X_{vol\%}$) of all coating samples during the 60 days of immersion are calculated by the Eq. (1) and are depicted in Fig. 10b. For the neat epoxy coating, the water uptake value increased quickly and reached to 7.4 vol% after 60 days of immersion.

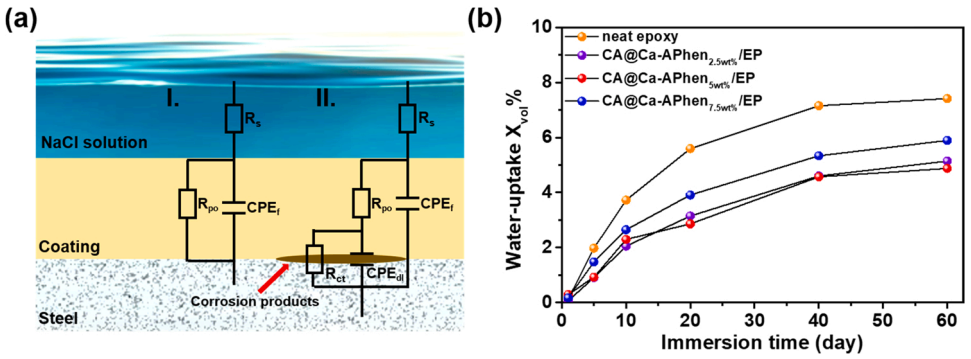

Fig. 10. (a) Equivalent electrical circuit utilized for fitting the EIS result of the intact coatings and (b) water uptake ($X_{vol\%}$) for different coated samples versus immersion time.

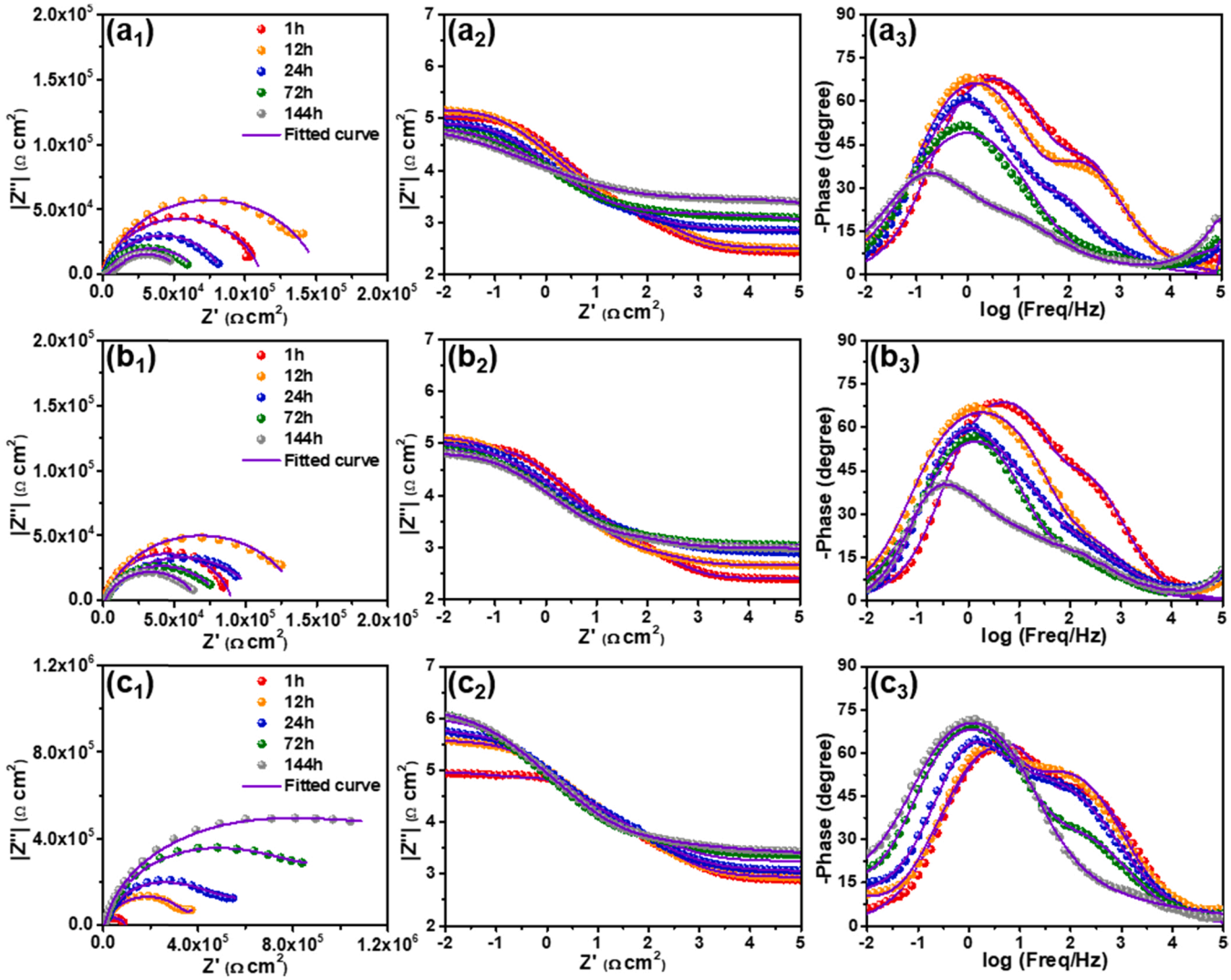

Fig. 11. Nyquist plots (a_1-c_1) and Bode plots (a_2-c_2 and a_3-c_3) of the scratched neat epoxy coating (a_1, a_2 and a_3), CA@$Ca_{5\ wt\%}$/EP coating (b_1, b_2 and b_3), and CA@Ca-$APhen_{5\ wt\%}$/EP coating (c_1, c_2 and c_3) during 144 h of immersion in 3.5 wt% NaCl solution; Fitted curves were added in the Nyquist plots and Bode plots (purple lines).

However, we found that the composite coatings with microcontainers obtain a lower $X_{vol\%}$ value (4.9–5.8 vol%) after an immersion time of 60 days, revealing notably improved barrier properties.

3.4. Active corrosion protection performance of the CA@Ca-APhen/EP coating

CA@Ca-$APhen_{5\ wt\%}$/EP coating was chosen for the study of the active corrosion protection effect considering its best barrier

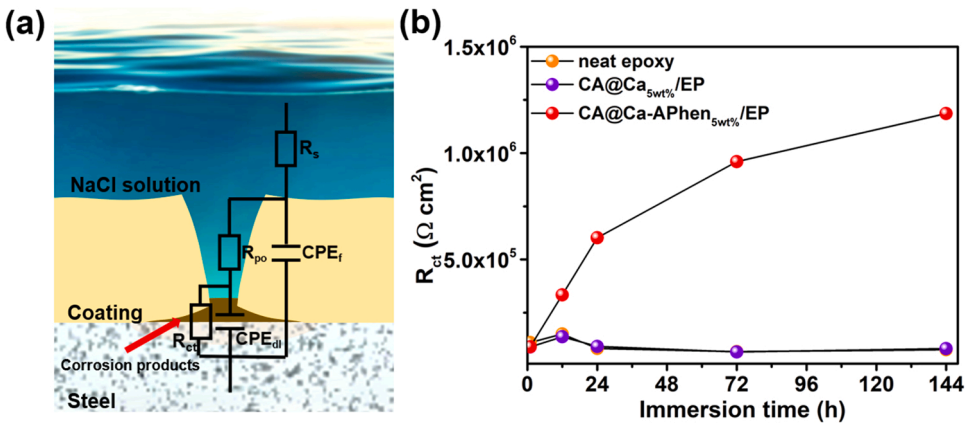

Fig. 12. Equivalent electrical circuit (a) utilized for fitting the EIS results of scratched coatings; (b) The variation of R_{ct} values of the scratched neat epoxy coating, CA@$Ca_{5\ wt\%}$/EP coating and CA@Ca-$APhen_{5\ wt\%}$/EP coating versus immersion time.

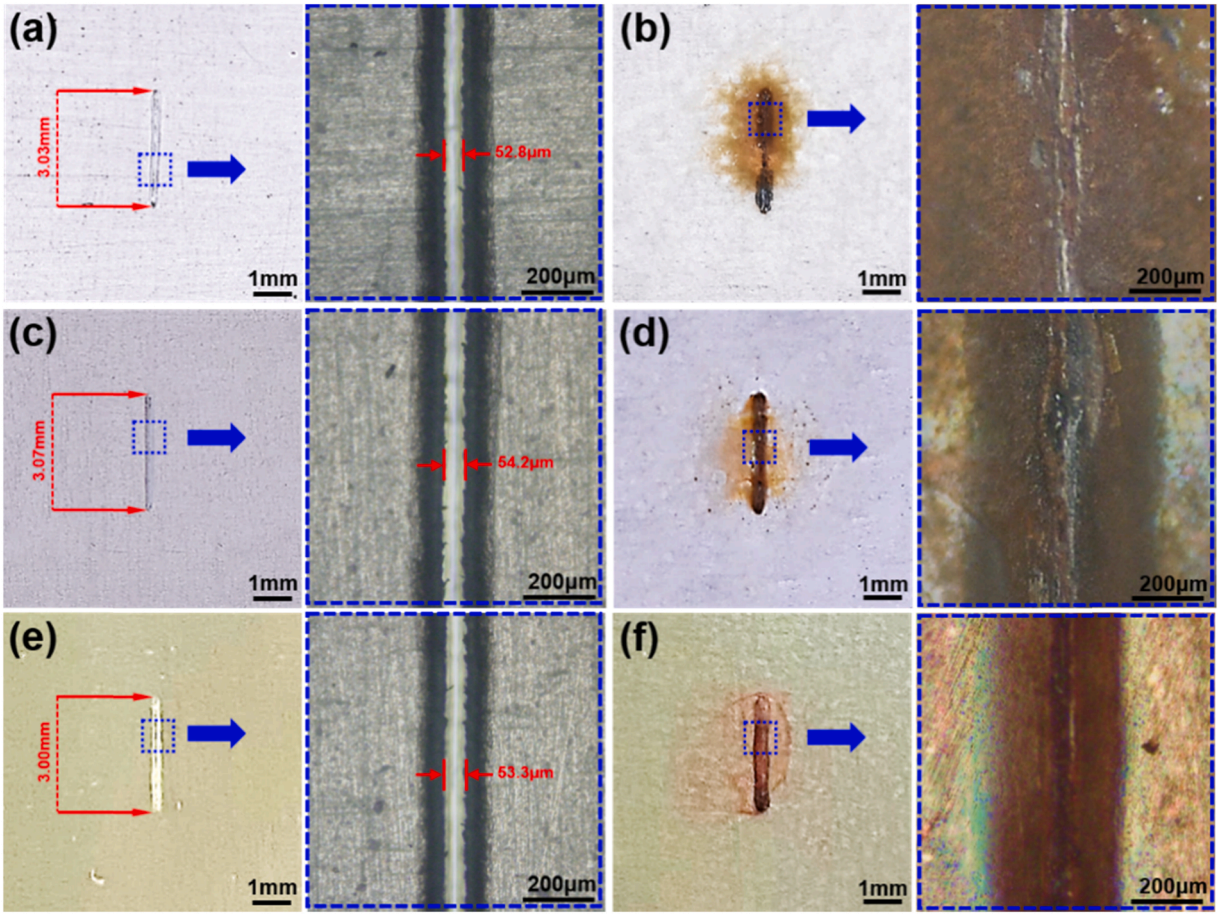

Fig. 13. Optical images of the scratched neat epoxy coating (a and b), CA@$Ca_{5\ wt\%}$/EP coating (c and d), and CA@Ca-$APhen_{5\ wt\%}$/EP coating (e and f) before and after 144 h of immersion in 3.5 wt% NaCl solution.

performance as demonstrated in Fig. 9. Prior to EIS measurements in 3.5 wt% NaCl solution, artificial through-coating scratches (~3 mm in length and ~50 μm in width) were made in the different coatings by a scalpel. Fig. 11 shows the Nyquist and Bode plots of the neat epoxy coating, the CA@$Ca_{5\ wt\%}$/EP coating, and the CA@Ca-$APhen_{5\ wt\%}$/EP coating. From the phase angle plots in Fig. 11a_3-c_3, two peaks can be distinguished roughly. The peak in the medium-frequency region (10^1-10^3 Hz) is mainly attributed to the pore plugging process of the corrosion products in the defect area [60]. The peak in the low frequency (10^{-2}~10^1 Hz) can be assigned to the charge transfer process at the metal surface [20]. The $|Z|_{f=10mHz}$ value of the coating containing the 5 wt% CA@Ca-APhen microcontainers is similar to that of the neat epoxy coating or the one containing the empty CA@Ca microcontainers after 1 h of immersion. The $|Z|_{f=10mHz}$ values of all three coatings slightly increased after 12 h of immersion, which can be attributed to the clogging of the scratch by corrosion products. After that, the $|Z|_{f=10mHz}$ values of the neat epoxy coating and CA@$Ca_{5\ wt\%}$/EP coating decreased steadily, which could be ascribed to the uninhibited corrosion in the

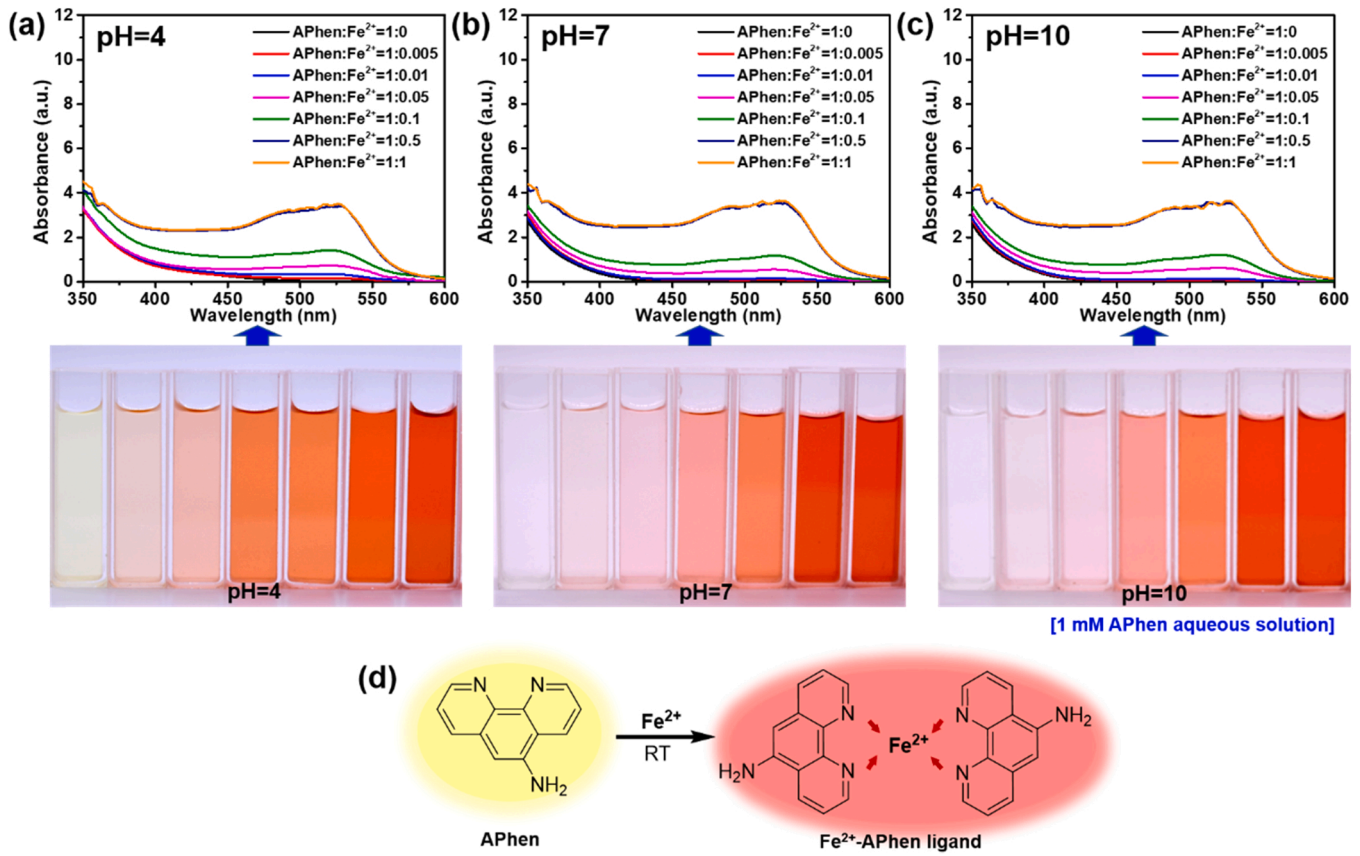

Fig. 14. (a-c) UV–vis spectra and optical images of APhen solution with the addition of different amounts of Fe^{2+} ions at the pH of 4, 7 and 10; (d) The ligand formed between APhen and Fe^{2+} ions.

coating damage. In contrast, the $|Z|_{f=10mHz}$ value of CA@Ca-APhen$_{5\ wt\%}$/EP coatings increased from $9.13 \times 10^4\ \Omega{\cdot}cm^2$ after 1 d to $1.19 \times 10^6\ \Omega{\cdot}cm^2$ after 144 h due to the release of APhen as a corrosion inhibitor, revealing an active corrosion protection effect.

The EIS results are also analyzed by an equivalent electrical circuit shown in Fig. 12a, which is a commonly used circuit to describe corrosion in a damaged coating region [61]. As shown in Fig. 12a, the corrosive species penetrate into the coating's defect and reach the metal surface, the corrosion reaction occurs instantaneously at the metal surface and rapidly generates corrosion products. Two time constants appear to reflect the pore plugging of corrosion products and the electron transfer related to the dissolution of the metal [20]. The evolution of R_{ct} values represents the difficulty in electron transfer on the steel substrate and can be used to compare the protection efficiency of different coatings (Fig. 12b) [62]. A higher R_{ct} value reflects a lower corrosion rate and thus a higher corrosion protection efficiency for the coating [63]. In the early stage of immersion, the R_{ct} value of the neat epoxy coating and the coating containing empty CA@Ca microcontainers showed a slight increase. With the extended immersion time, the R_{ct} value decreased because of the continuous deterioration of the scratched area. After 144 h of immersion, the R_{ct} values of the scratched neat epoxy coating and the coating containing empty CA@Ca microcontainers were as low as $7.51 \times 10^4\ \Omega\ cm^2$ and $7.80 \times 10^4\ \Omega\ cm^2$, respectively. In comparison, the R_{ct} values of the CA@Ca-APhen$_{5\ wt\%}$/EP coating showed a continuous increasing trend during the immersion and reached to $1.20 \times 10^6\ \Omega\ cm^2$ after 144 h of immersion.

Besides, Fig. 13a-f show the morphology of the coating scratches before the immersion and after 144 h of immersion in 3.5 wt% NaCl solution. A high degree of corrosion spreading and a large amount of corrosion products were found in the artificial scratch on the neat epoxy coating (Fig. 13b) or the coating containing empty CA@Ca microcontainers (Fig. 13d) after 144 h of immersion. In Fig. 13f, however, the scratch on the CA@Ca-APhen$_{5\ wt\%}$/EP coating showed relatively little rust in and around the scratch after 144 h of immersion, indicating corrosion on the exposed steel substrate was well inhibited. Noticeably, the scratch could show a distinct red color to report the corrosion activities.

3.5. *Self-sensing effect to corrosion damage in CA@Ca-APhen/EP coating*

Fig. 14a-c shows the UV–vis spectra of 1 mM APhen aqueous solutions with the addition of different amounts of $FeCl_2$ under the different pH conditions. After mixing 0.1 mM $FeCl_2$ solution and 1 mM APhen solution, a clear band at 520 nm was observed, which was related to the formation of a Fe^{2+}-APhen complex ($[Fe(APhen)_3]^{2+}$) (Fig. 14a-c) [64]. Besides, the strength of the absorbance corresponding to $[Fe(APhen)_3]^{2+}$ enhanced gradually with a higher $FeCl_2$ concentration. According to Fig. 14**c**, with a higher concentration of Fe^{2+} ions, the color of the APhen solution changed from light yellow to red. A prominent red color could be observed at the Fe^{2+} ion concentration as low as only 0.5 mM. The colors of the mixed solutions did not show significant difference within the range of pH 4–10, demonstrating the stability of the Fe^{2+}-APhen complex. These results indicated that the low concentration of Fe^{2+} ions can be readily detected in the presence of APhen at different pH conditions. Thus, the APhen molecules may serve as an effective sensor to probe the generation of Fe^{2+} ions from early metal corrosion.

To investigate the corrosion warning ability, the neat epoxy coating and the coating with the addition of 5 wt% CA@Ca-APhen microcontainers were scratched and salt spray exposed for different periods (Fig. 15). From Fig. 15a, there is almost no color change observed at the scratches for the neat epoxy coating within the first hour of the salt spray

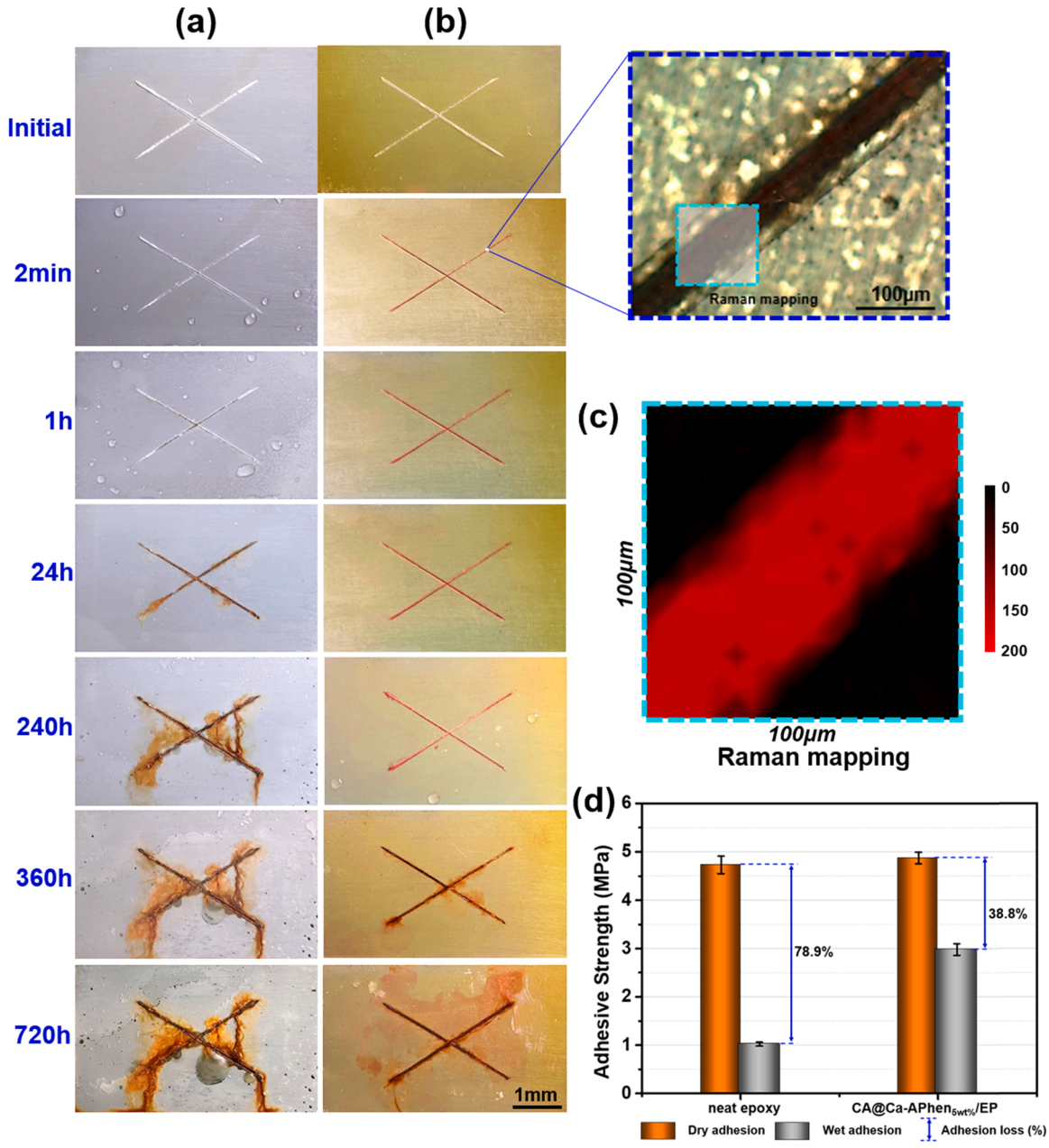

Fig. 15. Optical images of the scratched coatings after salt spray tests (a) neat epoxy and (b) CA@Ca-APhen$_{5\ wt\%}$/EP coating; (c) Raman intensity mapping for Fe^{2+}-APhen complex at 1513 cm^{-1} in the scratch on coated steel after 2 min of salt spray exposure; (d) The adhesion strength values of the neat epoxy and CA@Ca-APhen$_{5\ wt\%}$/EP coating before and after 720 h of salt spray exposure.

test. After 24 h, some corrosion products visible to the naked eye appeared at the scratched area. In contrast, the damaged region of the CA@Ca-APhen$_{5\ wt\%}$/EP coating exhibits a red color within only 2 min as an early indication of the corrosion onset and the intensity of the color significantly increased during the 1 h of salt spray testing (Fig. 15b). This phenomenon indicated that the Fe^{2+} ions generated from the corrosion process (anodic reaction) in the scratched area recombined with the released APhen molecules to form a red-color complex. Furthermore, from the Raman spectrum at the damage position (Fig. S4), it can be seen that the feature peaks at 1188, 1216, 1459 and 1513 cm^{-1} are observed with the presence of the red substances, confirming the generation of Fe^{2+}-APhen complex ($[Fe(APhen)_3]^{2+}$) [19]. According to Fig. S4, the Raman mapping signal at 1513 cm^{-1} is one of the main characteristic peaks of the Fe^{2+}-APhen complex. Fig. 15**c** shows the mapping of the intensity of the peak at 1513 cm^{-1} over the 0.1 μm^2 of the scratch region. The map shows a strong signal of the Fe^{2+}-APhen complex along the scratch after only 2 min. With the extension of the salt spray time, the color became more pronounced at the damaged position by visual inspection. These observations demonstrated that the coating can locate early corrosion with a rapid response of red color, which is highly useful for timely corrosion detection, repair and maintenance in practice.

Furthermore, as the salt spray exposure time increased to 720 h, the optical image showed large-scale coating delamination and a large amount of corrosion products at the scratch for the neat epoxy coating (Fig. 15a). In comparison, the epoxy coating that contained 5 wt% CA@Ca-APhen microcontainers showed little corrosion product but a prominent red color in the scratch (Fig. 15b). The colored region spreads around the scratch underneath the intact coating region, which may be attributed to the coating delamination. The results above demonstrate

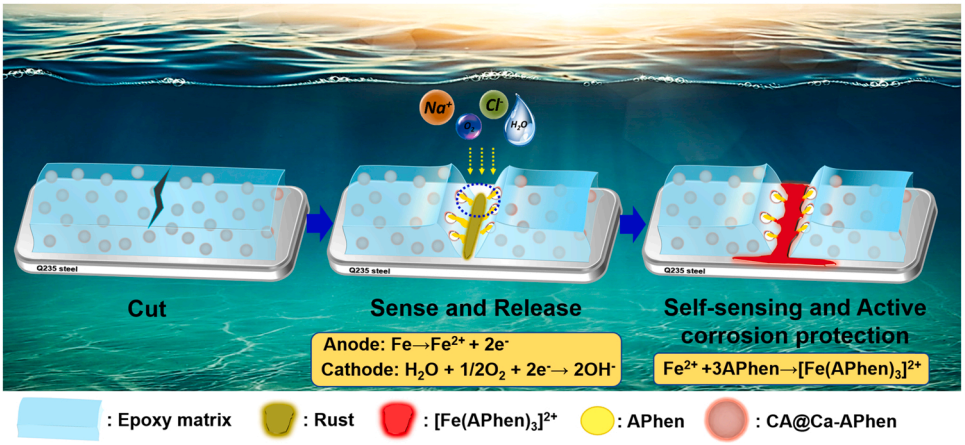

Fig. 16. Schematic illustration of the self-sensing and active corrosion protection process of the CA@Ca-APhen/EP coating.

that the addition of CA@Ca-APhen microcontainers can also give an obvious alarm of the corrosion situation under the coating, which is beneficial for accurate location and timely repairs of coating/corrosion damages.

As a main indicator of coating performance, adhesion strength can be measured via a pull-off test. Fig. 15d showed the adhesion strength/loss values of intact neat epoxy coating and CA@Ca-APhen$_{5\ wt\%}$/EP coating before and after the 720 h salt spray test. Before the salt spray test, the two samples had similar adhesion strength (neat epoxy coating: 4.73 MPa; CA@Ca-APhen$_{5\ wt\%}$/EP coating: 4.87 MPa), suggesting that the introduction of 5 wt% CA@Ca-APhen microcontainers did not affect the adhesion of the epoxy coating to the steel substrate. In practice, coatings are often exposed to a wet corrosion environment. Therefore, the better evaluation criteria of corrosion protection are the wet adhesion strength and the adhesion loss of coating which was estimated from the difference between the original adhesion strength and the wet adhesion strength after salt spray test in this study. The neat epoxy coating had a significant adhesion loss of 78.9% whereas the CA@Ca-APhen$_{5\ wt\%}$/EP coating showed an adhesion loss of 38.8%. These results demonstrate that the addition of 5 wt% CA@Ca-APhen microcontainers could induce a more durable adhesion of the coating onto the steel in corrosive environment, which could be attributed to the inhibition effect of APhen towards underfilm corrosion.

3.6. Smart corrosion protection mechanism of the CA@Ca-APhen/EP coating

Fig. 16 depicts the schematic illustration of self-sensing and active corrosion protection mechanism of the composite coating system. When the coating is damaged in the course of service, the steel substrate may be exposed to various corrosive species, such as chlorides, in a wet atmospheric environment providing all prerequisites for corrosion to occur. The homogeneous distribution of microcontainers encapsulated by polyelectrolyte shells in the coating matrix ensures the adequate presence of the microcontainers at the coating-damage interface (Fig. S3a) in order to quickly response to the occurrence of corrosion. The polyelectrolyte shell, composed of oppositely weakly charged polyelectrolyte, is pH sensitive, and enables the controllable release of corrosion inhibitors by regulating its permeability [65]. The changes in local pH due to corrosion cause the increasing permeability of the chitosan/alginate polyelectrolyte shell stimulating the release of APhen molecules from the microcontainers. The APhen molecules released from the microcontainers can react with Fe^{2+} to form a red complex at the exposed steel surface, which can not only provide an early warning of corrosion onset but also inhibit significant corrosion propagation.

4. Conclusions

In summary, the work reported the development of a smart coating that integrated self-sensing and active corrosion protection capabilities based on a novel pH-sensitive $CaCO_3$ microcontainer containing APhen molecules as both indicator and inhibitor of corrosion. The main conclusions from this study are as follows.

1) The CA@Ca microcontainer had a good drug loading capacity (~20.1 wt%) and could release APhen in a controlled fashion responding to pH variation. The corrosion of the Q235 steel was well inhibited in the presence of 100 mg/L CA@Ca-APhen microcontainers after 12 h immersion in the 3.5 wt% NaCl solutions with the initial pH values of 4, 7 and 10. The Raman spectra confirmed that the corrosion inhibition was attributed to the formation of Fe^{2+}-APhen complex.
2) The EIS results of the intact CA@Ca-APhen$_{5\ wt\%}$/EP coating showed an excellent barrier performance; The $|Z|_{10mHz}$ value of the composite coating slightly reduced from 6.92×10^{10} to 9.77×10^{9} $\Omega \cdot cm^2$ after 60 days of immersion; at this time, the water-uptake of the coating was 4.9–5.8 vol%.
3) The $|Z|_{10mHz}$ value of the scratched coating that contained 5 wt% CA@Ca-APhen microcontainers increased from 9.13×10^{4} to 1.19×10^{6} $\Omega \cdot cm^2$ after 144 h of immersion in 3.5 wt% NaCl solution, demonstrating an active corrosion protection effect.
4) From the results of salt spray test and Raman analysis, the APhen molecules were found to rapidly release from the scratch interface of the CA@Ca-APhen$_{5\ wt\%}$/EP coating and react with the Fe^{2+} ions to generate a distinct red deposit within 2 min. The CA@Ca-APhen$_{5\ wt\%}$/EP coating exhibited a stable coloration and little corrosion products after 720 h of salt spray test. The adhesion loss of the CA@Ca-APhen$_{5\ wt\%}$/EP coating after the salt spray test was 38.8%, which was much lower than that of the neat epoxy coating (78.9%).

CRediT authorship contribution statement

Tong Liu: Conceptualization, Methodology, Investigation, Writing – original draft. **Dawei Zhang:** Supervision, Conceptualization, Methodology, Writing – review & editing. **Lingwei Ma:** Investigation, Writing – review & editing. **Yao Huang:** Investigation. **Xiangping Hao:** Writing – review & editing. **Herman Terryn:** Methodology, Writing – review & editing. **Arjan Mol:** Methodology, Writing – review & editing. **Xiaogang Li:** Supervision. All authors contributed to the discussion of the work.

Declaration of Competing Interest

The authors declare that they have no known competing financial

interests or personal relationships that could have appeared to influence the work reported in this paper.

Data Availability

The data that support the findings of this study are available upon reasonable request from the authors.

Acknowledgments

This work was supported by the National Natural Science Foundation of China (No. 51771029) and the Fundamental Research Funds for the Central Universities (FRF-BD-20–28A2).

Appendix A. Supporting information

Supplementary data associated with this article can be found in the online version at doi:10.1016/j.corsci.2022.110254.

References

[1] X. Li, D. Zhang, Z. Liu, Z. Li, C. Du, C. Dong, Materials science: share corrosion data, Nature 527 (2015) 441–442.
[2] B. Hou, X. Li, X. Ma, C. Du, D. Zhang, M. Zheng, W. Xu, D. Lu, F. Ma, The cost of corrosion in China, npj Mater. Degrad. 1 (2017) 1–10.
[3] F. Zhang, P. Ju, M. Pan, D. Zhang, Y. Huang, G. Li, X. Li, Self-healing mechanisms in smart protective coatings: a review, Corros. Sci. 144 (2018) 74–88.
[4] S. An, M.W. Lee, A.L. Yarin, S.S. Yoon, A review on corrosion-protective extrinsic self-healing: comparison of microcapsule-based systems and those based on core-shell vascular networks, Chem. Eng. J. 344 (2018) 206–220.
[5] L. Ma, C. Ren, J. Wang, T. Liu, H. Yang, Y. Wang, Y. Huang, D. Zhang, Self-reporting coatings for autonomous detection of coating damage and metal corrosion: a review, Chem. Eng. J. (2020), 127854.
[6] T. Liu, L. Ma, X. Wang, J. Wang, H. Qian, D. Zhang, X. Li, Self-healing corrosion protective coatings based on micro/nanocarriers: a review, Corros. Commun. 1 (2021) 18–25.
[7] C. Tsai, F. Mansfeld, Determination of coating deterioration with EIS: Part II. Development of a method for field testing of protective coatings, Corrosion 49 (1993).
[8] D. Ghosh, R. Kumar, A. Ganguli, A. Mukherjee, Nondestructive evaluation of rebar corrosion–induced damage in concrete through ultrasonic imaging, J. Mater. Civ. Eng. 32 (2020), 04020294.
[9] Z. Li, Z. Jin, X. Xu, T. Zhao, P. Wang, Z. Li, Combined application of novel electromagnetic sensors and acoustic emission apparatus to monitor corrosion process of reinforced bars in concrete, Constr. Build. Mater. 245 (2020), 118472.
[10] R. Wu, H. Zhang, R. Yang, W. Chen, G. Chen, Nondestructive testing for corrosion evaluation of metal under coating, J. Sens. 2021 (2021), 6640406.
[11] K. Dragan, Analysis of the possibility to assess the occurrence of hidden corrosion in lap joints using active thermography, Fatigue Aircr. Struct. (2011) 53–56.
[12] I. Sousa, M.C. Quevedo, A. Sushkova, M.G.S. Ferreira, J. Tedim, Chitosan microspheres as carriers for ph-indicating species in corrosion sensing, Macromol. Mater. Eng. 305 (2020), 1900662.
[13] J. Zhang, G. Frankel, Corrosion-sensing behavior of an acrylic-based coating system, Corrosion 55 (1999) 957–967.
[14] T.L. Galvao, I. Sousa, M. Wilhelm, J. Carneiro, J. Opršal, H. Kukačková, V. Špaček, F. Maia, J.R. Gomes, J. Tedim, Improving the functionality and performance of AA2024 corrosion sensing coatings with nanocontainers, Chem. Eng. J. 341 (2018) 526–538.
[15] G. Dhole, G. Gunasekaran, S. Singh, M. Vinjamur, Smart corrosion sensing phenanthroline modified alkyd coatings, Prog. Org. Coat. 89 (2015) 8–16.
[16] M. Wilhelm, M.C. Quevedo, A. Sushkova, T.L. Galvão, A. Bastos, M. Ferreira, J. Tedim, Hexacyanoferrate-intercalated layered double hydroxides as nanoadditives for the detection of early-stage corrosion of steel: the revival of prussian blue, Eur. J. Inorg. Chem. 2020 (2020) 2063–2073.
[17] M.J. Robb, W. Li, R.C. Gergely, C.C. Matthews, S.R. White, N.R. Sottos, J.S. Moore, A robust damage-reporting strategy for polymeric materials enabled by aggregation-induced emission, ACS Cent. Sci. 2 (2016) 598–603.
[18] X. Zheng, Q. Wang, Y. Li, S. Xu, Y. Li, Fabrication of self-reactive microcapsules as color visual sensing for damage reporting, J. Mater. Sci. 55 (2020) 8861–8867.
[19] C. Liu, H. Wu, Y. Qiang, H. Zhao, L. Wang, Design of smart protective coatings with autonomous self-healing and early corrosion reporting properties, Corros. Sci. 184 (2021), 109355.
[20] T. Liu, H. Zhao, D. Zhang, Y. Lou, L. Huang, L. Ma, X. Hao, L. Dong, F. Rosei, W. M. Lau, Ultrafast and high-efficient self-healing epoxy coatings with active multiple hydrogen bonds for corrosion protection, Corros. Sci. 187 (2021), 109485.
[21] S.R. White, N.R. Sottos, P.H. Geubelle, J.S. Moore, S. Viswanathan, Autonomic healing of polymer composites, Nature 409 (2001) 794–797.
[22] M. Behzadnasab, S.M. Mirabedini, M. Esfandeh, R.R. Farnood, Evaluation of corrosion performance of a self-healing epoxy-based coating containing linseed oil-filled microcapsules via electrochemical impedance spectroscopy, Prog. Org. Coat. 105 (2017) 212–224.
[23] D. Fix, D.V. Andreeva, Y.M. Lvov, D.G. Shchukin, H. Möhwald, Application of inhibitor-loaded halloysite nanotubes in active anti-corrosive coatings, Adv. Funct. Mater. 19 (2009) 1720–1727.
[24] D.G. Shchukin, H. Möhwald, Surface-engineered nanocontainers for entrapment of corrosion inhibitors, Adv. Funct. Mater. 17 (2007) 1451–1458.
[25] L. Gao, J. He, J. Hu, C. Wang, Photo-responsive self-healing polymer composite with photo-absorbing hybrid microcapsules, ACS Appl. Mater. Interfaces 7 (2015) 25546–25552.
[26] Y.K. Song, Y.H. Jo, Y.J. Lim, S.Y. Cho, H.C. Yu, B.C. Ryu, S.I. Lee, C.M. Chung, Sunlight-induced self-healing of a microcapsule-type protective coating, ACS Appl. Mater. Interfaces 5 (2013) 1378–1384.
[27] W. Lv, J. Feng, W. Yan, C.F.J. Faul, Self-assembly and pH response of electroactive liquid core–tetra(aniline) shell microcapsules, J. Mater. Chem. B 2 (2014) 4720–4725.
[28] D.V. Andreeva, D. Fix, H. Möhwald, D.G. Shchukin, Self-healing anticorrosion coatings based on ph-sensitive polyelectrolyte/inhibitor sandwichlike nanostructures, Adv. Mater. 20 (2008) 2789–2794.
[29] W. Wang, L. Xu, X. Li, Z. Lin, E. An, Self-healing mechanisms of water triggered smart coating in seawater, J. Mater. Chem. A 2 (2014) 1914–1921.
[30] K.S. Toohey, N.R. Sottos, J.A. Lewis, J.S. Moore, S.R. White, Self-healing materials with microvascular networks, Nat. Mater. 6 (2007) 581–585.
[31] A. Dolatkhah, L.D. Wilson, Saline-responsive and hydrogen bond gating effects in self-healing polyaniline, ACS Appl. Polym. Mater. 2 (2020) 2311–2318.
[32] P.P.A.C. Santos, S. Jesus, F. Veiga, Y. Lvov, A.J. Ribeiro, Sonication-assisted layer-by-layer assembly for low solubility drug nanoformulation, ACS Appl. Mater. Interfaces 7 (2015) 11972–11983.
[33] J.C. Antunes, C.L. Pereira, M. Molinos, F. Ferreira-Da-Silva, M. Dessì, A. Gloria, L. Ambrosio, R.M. GonAlves, M.A. Barbosa, Layer-by-layer self-assembly of chitosan and poly(γ-glutamic acid) into polyelectrolyte complexes, Biomacromolecules (2011) 4183–4185.
[34] E.V. Skorb, D.V. Andreeva, Layer-by-Layer approaches for formation of smart self-healing materials, Polym. Chem. 4 (2013) 4834–4845.
[35] M.L. Zheludkevich, D.G. Shchukin, K.A. Yasakau, H. Möhwald, M. Ferreira, Anticorrosion coatings with self-healing effect based on nanocontainers impregnated with corrosion inhibitor, Chem. Mater. 19 (2007) 402–411.
[36] D.G. Shchukin, M. Zheludkevich, K. Yasakau, S. Lamaka, M.G.S. Ferreira, Layer-by-layer assembled nanocontainers for self-healing corrosion protection, Adv. Mater. 18 (2006) 1672–1678.
[37] Z. Zheng, M. Schenderlein, X. Huang, N.J. Brownbill, F. Blanc, D. Shchukin, Influence of functionalization of nanocontainers on self-healing anticorrosive coatings, ACS Appl. Mater. Interfaces 7 (2015) 22756–22766.
[38] M. Cui, D.I. Njoku, B. Li, L. Yang, Z. Wang, B. Hou, Y. Li, Corrosion protection of Aluminium Alloy 2024 through an epoxy coating embedded with smart microcapsules: The responses of smart microcapsules to corrosive entities, Corros. Commun. 1 (2021) 1–9.
[39] D.I. Njoku, B. Li, M.S. Khan, U.P. Chinonso, C.N. Njoku, I.B. Onyeachu, Y. Li, Quadruple-action coatings provided by doping epoxy with inhibitor laden clay nanotubes functionalized with layer-by-layer of cross-bridged chitosan and anionic polyelectrolytes, Prog. Org. Coat. 157 (2021), 106312.
[40] X. Liu, D. Zhang, P. Hou, J. Pan, X. Zhao, B. Hou, Preparation and characterization of polyelectrolyte-modified attapulgite as nanocontainers for protection of carbon steel, J. Electrochem. Soc. 165 (2018) C907.
[41] N.M. Hettiarachchi, R.T. De Silva, M.P.G. Mantilaka, P. Pasbakhsh, K.N. De Silva, G.A. Amaratunga, Synthesis of calcium carbonate microcapsules as self-healing containers, RSC Adv. 9 (2019) 23666–23677.
[42] Y. Huang, L. Deng, P. Ju, L. Huang, H. Qian, D. Zhang, X. Li, H.A. Terryn, J.M. C. Mol, Triple-action self-healing protective coatings based on shape memory polymer (SMP) containing dual-function microspheres, ACS Appl. Mater. Interfaces 10 (2018) 23369–23379.
[43] L. Ma, J. Wang, D. Zhang, Y. Huang, L. Huang, P. Wang, H. Qian, X. Li, H.A. Terryn, J.M.C. Mol, Dual-action self-healing protective coatings with photothermal responsive corrosion inhibitor nanocontainers, Chem. Eng. J. (2020), 127118.
[44] D. Brasher, A. Kingsbury, Electrical measurements in the study of immersed paint coatings on metal. I. Comparison between capacitance and gravimetric methods of estimating water-uptake, J. Appl. Chem. 4 (1954) 62–72.
[45] V.N. Nguyen, F.X. Perrin, J.L. Vernet, Water permeability of organic/inorganic hybrid coatings prepared by sol–gel method: a comparison between gravimetric and capacitance measurements and evaluation of non-Fickian sorption models, Corros. Sci. 47 (2005) 0–412.
[46] Y. Shang, Y. Cui, R. Shi, P. Yang, J. Wang, Y. Wang, Regenerated WO2. 72 nanowires with superb fast and selective adsorption for cationic dye: kinetics, isotherm, thermodynamics, mechanism, J. Hazard. Mater. 379 (2019), 120834.
[47] C. Pesquera, F. González, I. Benito, C. Blanco, S. Mendioroz, J. Pajares, Passivation of a montmorillonite by the silica created in acid activation, J. Mater. Chem. 2 (1992) 907–911.
[48] H.A. Al-Hosney, V.H. Grassian, Water, sulfur dioxide and nitric acid adsorption on calcium carbonate: a transmission and ATR-FTIR study, Phys. Chem. Chem. Phys. 7 (2005) 1266–1276.
[49] C. Zheng, H. Ren, Z. Cui, F. Chen, G. Hong, Synthesis and characterization of nano-scale Terbium (III)-trimesic acid (TMA)-1,10-phenanthroline(phen) luminescent complex, J. Alloy. Compd. 477 (2009) 333–336.
[50] H.L. Wu, X.X. Hou, C. Branford White, X.Z. Sun, L. Tao, S. Um-I-Zahra, L.-M. Zhu, Drug-loaded microparticles prepared by the one-step deposition of calcium carbonate/alginate onto cotton fabrics, J. Appl. Polym. Sci. 132 (2015) 42618.

[51] I. Sousa, M.C. Quevedo, A. Sushkova, M.G. Ferreira, J. Tedim, Chitosan microspheres as carriers for pH–indicating species in corrosion sensing, Macromol. Mater. Eng. 305 (2020), 1900662.
[52] M. Wang, L. Wu, Q. Hu, Y. Yang, Application of magnetic nanoparticles coated with sodium dodecyl sulfate and modified with 2-(5-bromo-2-pyridylazo)-5-diethyl aminophenol as a novel adsorbent for dispersive-magnetic solid-phase extraction and determination of palladium in soil samples, Environ. Sci. Pollut. Res. 25 (2018) 8340–8349.
[53] W. Mo, H. Liu, H. Xiong, M. Li, G. Li, Preparation of CuCl/1, 10-phenanthroline immobilized on polystyrene and catalytic performance in oxidative carbonylation of methanol, Appl. Catal. A-Gen. 333 (2007) 172–176.
[54] M. Theerasilp, D. Crespy, Halochromic polymer nanosensors for simple visual detection of local pH in coatings, Nano Lett. 21 (2021) 3604–3610.
[55] H. Shi, L. Wu, J. Wang, F. Liu, E.-H. Han, Sub-micrometer mesoporous silica containers for active protective coatings on AA 2024-T3, Corros. Sci. 127 (2017) 230–239.
[56] M.L. Zheludkevich, J. Tedim, M.G.S. Ferreira, "Smart" coatings for active corrosion protection based on multi-functional micro and nanocontainers, Electrochim. Acta 82 (2012) 314–323.
[57] N.Y. Abu-Thabit, A.S. Hamdy, Stimuli-responsive polyelectrolyte multilayers for fabrication of self-healing coatings–a review, Surf. Coat. Technol. 303 (2016) 406–424.
[58] S.J. Oh, D. Cook, H. Townsend, Characterization of iron oxides commonly formed as corrosion products on steel, Hyperfine Inter. 112 (1998) 59–66.
[59] T. Ohtsuka, Raman spectra of passive films of iron in neutral borate solution, Mater. Trans., JIM 37 (1996) 67–69.
[60] C. Oliveira, M. Ferreira, Ranking high-quality paint systems using EIS. Part I: intact coatings, Corros. Sci. 45 (2003) 123–138.
[61] I. Dehri, M. Erbil, The effect of relative humidity on the atmospheric corrosion of defective organic coating materials: an EIS study with a new approach, Corros. Sci. 42 (2000) 969–978.
[62] T. Liu, Y. Liu, Y. Ye, J. Li, F. Yang, H. Zhao, L. Wang, Corrosion protective properties of epoxy coating containing tetraaniline modified nano-α-Fe_2O_3, Prog. Org. Coat. 132 (2019) 455–467.
[63] M. Aghili, M.K. Yazdi, Z. Ranjbar, S.H. Jafari, Anticorrosion performance of electro-deposited epoxy/ amine functionalized graphene oxide nanocomposite coatings, Corros. Sci. 179 (2021), 109143.
[64] L. Kozak, P. Niedzielski, W. Wachowiak, The tandem analytical method of flow injection diode array spectrophotometry and flame atomic absorption spectrometry (FI-DAD (vis)-FAAS) in iron speciation studies using 1, 10-phenanthroline complexes, Microchem. J. 110 (2013) 54–60.
[65] T. Chen, J.J. Fu, An intelligent anticorrosion coating based on pH-responsive supramolecular nanocontainers, Nanotechnology 23 (2012), 505705.